

Article

Zagamiite, $\text{CaAl}_2\text{Si}_{3.5}\text{O}_{11}$, the Hexagonal High-Pressure CAS Phase with Dominant Si, as a Mineral from Mars

Chi Ma ^{1,*}, Oliver Tschauer ^{2,*}, John R. Beckett ¹, Eran Greenberg ³ and Vitali B. Prakapenka ³

¹ Division of Geological and Planetary Sciences, California Institute of Technology, Pasadena, CA 91125, USA; beckett@caltech.edu

² Department of Geoscience, University of Nevada, Las Vegas, NV 89154, USA

³ Center for Advanced Radiation Sources, The University of Chicago, Argonne National Laboratory, Chicago, IL 60637, USA; erangre@gmail.com (E.G.); vitali@uchicago.edu (V.B.P.)

* Correspondence: chima@caltech.edu (C.M.); oliver.tschauer@unlv.edu (O.T.)

Abstract: Within the Ca-Al-silicate system, dense, layered hexagonal phases occur at high temperatures and pressures between 20 and 23 GPa. They have been observed both in nature and in experiments. In this study, we describe the endmember with a dominant sixfold coordinated Si as a mineral zagamiite (IMA 2015-022a). This new mineral identified in Martian meteorites has a general formula of $(\text{Ca,Na})(\text{Al,Fe,Mg})_2(\text{Si,Al},\square)_4\text{O}_{11}$, thus defining $\text{CaAl}_2\text{Si}_{3.5}\text{O}_{11}$ as a previously unknown endmember of the hexagonal CAS phases. Zagamiite assumes space group $P6_3/mmc$ with a unit cell of $a = 5.403(2) \text{ \AA}$, $c = 12.77(3) \text{ \AA}$, $V = 322.9(11) \text{ \AA}^3$, and $Z = 2$. Zagamiite contains significant Fe and Mg and a substantial deficit of Na relative to plagioclase of an equivalent Al/Si, suggesting that it was formed through crystallization from a melt that was derived from a plagioclase-dominant mixture of plagioclase and clinopyroxene above the solidus beyond 20 GPa.

Keywords: Zagamiite; $\text{CaAl}_2\text{Si}_{3.5}\text{O}_{11}$; CAS phase; high-pressure mineral; shock metamorphism; Martian meteorite; Zagami; NWA 856



Citation: Ma, C.; Tschauer, O.; Beckett, J.R.; Greenberg, E.; Prakapenka, V.B. Zagamiite, $\text{CaAl}_2\text{Si}_{3.5}\text{O}_{11}$, the Hexagonal High-Pressure CAS Phase with Dominant Si, as a Mineral from Mars. *Minerals* **2024**, *14*, 18. <https://doi.org/10.3390/min14010018>

Academic Editor: Roman Skála

Received: 19 October 2023

Revised: 13 December 2023

Accepted: 16 December 2023

Published: 22 December 2023



Copyright: © 2023 by the authors. Licensee MDPI, Basel, Switzerland. This article is an open access article distributed under the terms and conditions of the Creative Commons Attribution (CC BY) license (<https://creativecommons.org/licenses/by/4.0/>).

1. Introduction

The phase diagrams of the CAS (Ca-Al-Silicate) system and the extended (K,Na)-CAS system exhibit high-pressure phases that are quite different from those in the MAS (Mg-Al-Silicate) system. These include the hollandite-type phases lingunite [1], stöfflerite [2], and liebermanite [3], of which only the latter possesses a stability field as a pure phase, and the davemaoite [4] and Ca-ferrite-type phases at Earth's lower mantle pressures [5]. At intermediate pressures and at temperatures close to or at the solidus [6,7], a phase of hexagonal symmetry with octahedral layers as basic units [8–10] appears. Gautron et al. [10] synthesized this phase and determined the structure, referring to it as a 'hexagonal CAS-phase' with a formula of $\text{CaAl}_4\text{Si}_2\text{O}_{11}$ (hereafter, 'CAS phase' in distinction from the CAS-like minerals and the CAS system in general). In 2004, Beck et al. [11] used a Raman spectroscopy and electron probe microanalyses (EPMA) to report this phase from shocked Martian meteorites, including Zagami and NWA 856, with a formula of $(\text{Ca}_x\text{Na}_{1-x})\text{Al}_{3+x}\text{Si}_{3-x}\text{O}_{11}$. However, no structural analysis of the natural material was obtained, and, therefore, the occurrence was not reported as a new mineral species. In 2017, Ma et al. [12] characterized the composition and structure of two occurrences of the CAS phase in shock melt pockets in the basaltic shergottites Zagami and NWA 856, and these findings were accepted by the International Mineralogical Association (IMA) as defining the natural CAS phase as a new mineral species with the name zagamiite (IMA 2015-022a, [13]). Thereafter, several publications reported this mineral in natural shock-metamorphic occurrences, where it is commonly associated with shock melt pockets that entrain feldspathic material, or discussed its relationship with other high-pressure

minerals [2,3,14–19]. Donwilhelmsite, $\text{CaAl}_4\text{Si}_2\text{O}_{11}$, a lunar shock-metamorphic, high-pressure mineral [20], defines the Al-rich endmember of an isotypic, potentially isomorphic, series, and zagamiite, $\text{CaAl}_2\text{Si}_{3.5}\text{O}_{11}$, establishes the Si-rich endmember. In this study, we describe the structure, composition, and formation of zagamiite. The new mineral species received its name after the locality of the fall of the Zagami meteorite: Zagami, Nigeria.

2. Materials and Methods

The Zagami meteorite fell at Zagami, Katsina Province, Nigeria on 3 October 1962. The NWA 856 meteorite was found in Morocco in March, 2001. Both are Martian, rare earth-enriched, intersertal, basaltic shergottites. The type zagamiite from the Caltech Zagami section is deposited in the collections of the Smithsonian Institution's National Museum of Natural History, Washington DC, USA, registration number USNM 7619. This section also hosts type liebermannite (hollandite-type KAlSi_3O_8 [3]). The cotype zagamiite in Caltech's NWA 856 section is in E. Stolper's Martian Meteorite Collection of the Division of Geological and Planetary Sciences, California Institute of Technology, Pasadena, California 91125, USA. This NWA 856 section also hosts type stöfflerite (hollandite-type $(\text{Ca},\text{Na})(\text{Si},\text{Al})_4\text{O}_8$ [2]).

The Zagami meteorite consists mainly of pyroxene (mostly zoned augite and pigeonite) and maskelynite (shock-generated plagioclase glass), with ilmenite, titanomagnetite, baddeleyite, merrillite, apatite, and Fe sulfide as accessory minerals, plus shock melt veins and pockets including associated shock phases. The high-pressure metamorphic phases include zagamiite, liebermannite, lingunite, tuite, stishovite, and tissintite. The pyroxene (augite and pigeonite) and maskelynite are also the major phases in the NWA 856 meteorite. The accessory phases include ilmenite, titanomagnetite, chromite, baddeleyite, merrillite, apatite, and Fe sulfide, and there are scattered shock melt pockets. The high-pressure metamorphic phases include zagamiite, stöfflerite, and stishovite.

Field-emission scanning electron microscopy (FE-SEM), electron backscatter diffraction (EBSD), electron probe microanalysis (EPMA), and synchrotron X-ray diffraction (SXRD) were used to characterize the composition, the structure, and the petrography of the zagamiite and associated phases. The backscatter electron (BSE) imaging was performed using a ZEISS 1550VP FE-SEM. The EBSD analyses were attempted using an HKL EBSD system on a ZEISS 1550VP SEM, operated at 20 kV and 6 nA in a focused-beam mode with a 70° tilted stage and a variable pressure mode (25 Pa). The chemical analyses of the zagamiite and associated phases were carried out using a JEOL 8200 electron microprobe interfaced with the Probe for EPMA program from Probe Software, Inc. (Eugene, OR, USA) and operated in a focused-beam mode at 15 kV or 10 kV and 5 nA with a probe diameter of ~150 nm. The standards were anorthite ($\text{CaK}\alpha$, $\text{AlK}\alpha$, $\text{SiK}\alpha$), albite ($\text{NaK}\alpha$), microcline ($\text{KK}\alpha$), fayalite ($\text{FeK}\alpha$), forsterite ($\text{MgK}\alpha$), TiO_2 ($\text{TiK}\alpha$), and Mn_2SiO_4 ($\text{MnK}\alpha$). The quantitative elemental microanalyses were processed with the CITZAF correction procedure [21], and the analytical results are given in Table 1.

Table 1. EPMA data for type zagamiite in the Zagami and NWA 856.

Constituent wt%	Zagami <i>n</i> = 6 ^a	SD ^b	NWA 856 <i>n</i> = 8	SD
SiO ₂	56.95	0.98	56.22	1.40
Al ₂ O ₃	28.27	1.14	27.26	1.46
CaO	9.96	0.73	10.71	0.76
Na ₂ O	2.67	0.42	2.49	0.36
FeO	1.01	0.04	1.64	1.04
K ₂ O	0.44	0.06	0.39	0.10
MgO	0.06	0.03	0.24	0.17
TiO ₂	0.05	0.02	0.08	0.06
MnO	0.03	0.04	0.08	0.04
Total	99.45		99.10	
No. O atoms	11		11	
Si	3.51		3.50	
Al	2.05		2.00	
Ca	0.66		0.71	
Na	0.32		0.30	
Fe	0.05		0.09	
K	0.03		0.03	
Mg	0.01		0.02	
Ti	0.00		0.00	
Mn	0.00		0.00	
Sum cations	6.63		6.65	

^a *n* = number of analyses. ^b Errors given inside parentheses are one standard deviation of the mean based on all of the analyses.

3. Results

Zagamiite occurs within shock melt pockets in the Zagami and NWA 856 (Figures 1 and 2). A shock melt pocket in the Zagami, surrounded by augite, pigeonite, and maskelynite (An53; shock-generated plagioclase glass), contains zagamiite domains and stishovite-bearing regions. Tissintite (described as ‘tissintite II’ with a composition of (Ca,Mg,Na,□_{0.14})(Al,Fe,Mg)Si₂O₆ [22]) is scattered at the rim of the melt pocket (Figure 1). Stishovite was not observed within the zagamiite domains.

In the NWA 856 meteorite, zagamiite occurs along with regions of stishovite–zagamiite intergrowth in shock melt pockets, surrounded by augite, pigeonite, and maskelynite (An56) (Figure 2). Fine-grained stöfflerite formed from maskelynite occurs at the contact of some melt pockets (Figure 2a, [2]).

Zagamiite occurs as fine-grained prismatic crystals, from less than 50 nm × 100 nm to 400 nm × 1 μm in size (Figures 1b and 2b). The type areas are aggregates. It is colorless and transparent. The luster, streak, hardness, tenacity, cleavage, fracture, density, and optical properties could not be determined empirically because of the small grain size. The density, calculated from the unit cell volume, number of chemical formula units, and the empirical formula, as described below, is 3.79 and 3.81 g/cm³, respectively, in the Zagami and the NWA 856.

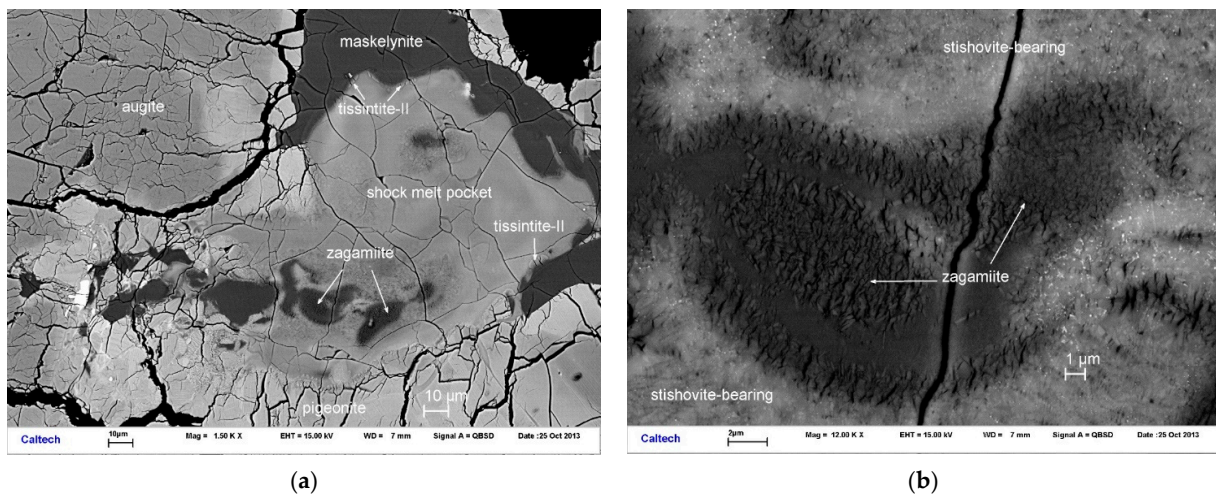


Figure 1. (a) Backscatter electron (BSE) image showing a zagamiite-bearing shock melt pocket in Zagami. (b) Enlarged BSE image of areas in Figure 1a revealing fine-grained zagamiite. Stishovite-bearing regions also contain zagamiite and quenched melt.

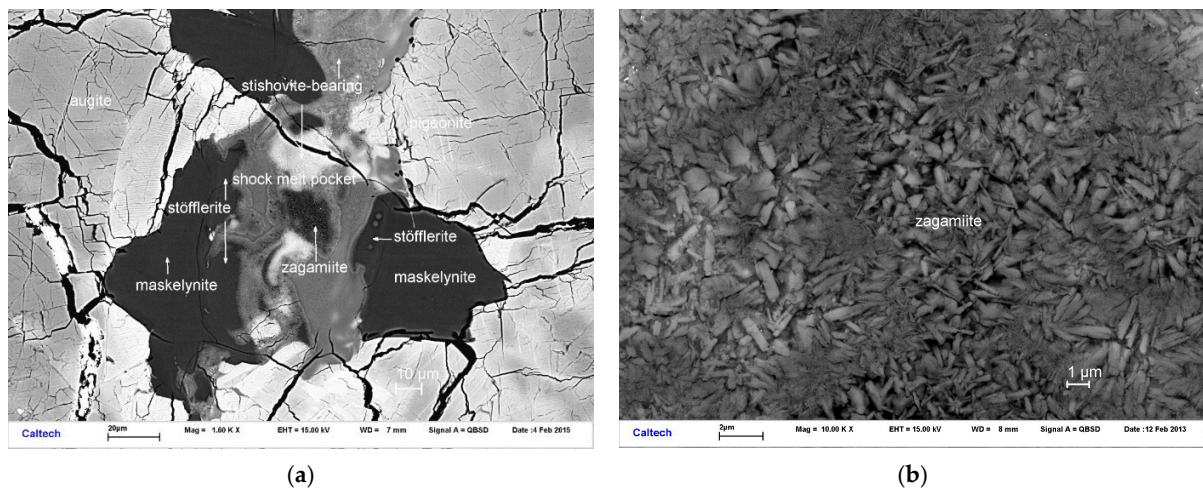


Figure 2. (a) BSE image showing a zagamiite-bearing shock melt pocket in NWA 856. (b) A cluster of zagamiite crystals in a different melt pocket in NWA 856.

The compositions (Table 1) of type zagamiite in the Zagami and the NWA 856 correspond to an empirical formula based on 11 oxygens apfu of $(\text{Ca}_{0.66}\text{Na}_{0.32}\text{K}_{0.03})(\text{Al}_{1.94}\text{Fe}_{0.05}\text{Mg}_{0.01})(\text{Si}_{3.51}\text{Al}_{0.11})\text{O}_{11}$ and $(\text{Ca}_{0.71}\text{Na}_{0.30}\text{K}_{0.03})(\text{Al}_{1.89}\text{Fe}_{0.09}\text{Mg}_{0.02})(\text{Si}_{3.50}\text{Al}_{0.11})\text{O}_{11}$, respectively. The compositions of zagamiite are different from those of the associated maskelynite. Zagamiite has a general formula of $(\text{Ca},\text{Na})(\text{Al},\text{Fe},\text{Mg})_2(\text{Si},\text{Al},\square)_4\text{O}_{11}$ and an endmember formula of $\text{CaAl}_2\text{Si}_{3.5}\text{O}_{11}$. The detailed analyses are given in Table 1.

The synchrotron diffraction data were collected at the undulator beamline 13-IDD (GSECARS, APS, Argonne National Laboratory), using a microfocused beam ($3 \times 4 \mu\text{m}^2$) of wavelength 0.4133 \AA and a MAR165 CCD area detector. The sample detector distance and geometric correction factors were determined using GSE-ADA [23]. The calibration was used for integrating the diffraction data with Dioptas [24].

Data were collected in transmission on the type material thin section. A diffraction frame was taken for the maskelynite through the resin-covered glass slide and used as the background frame. This pixel-by-pixel subtraction reduced the structured background and the vitreous signal without distorting the Bragg peak profiles or removing the crystalline diffraction signal. The synchrotron diffraction patterns of the zagamiite were powder-like for the given diffraction volume, as shown in Figure 3a. Based on the similarity of the EBSD

pattern of the zagamiite and the synthetic CAS phase $\text{CaAl}_4\text{Si}_2\text{O}_{11}$ [10], we examined the structure as follows. By using the structure model of Gautron et al. [10], we confirmed the close structural relations and the hexagonal metric of the zagamiite. However, zagamiite is distinct from the reported synthetic CAS phase in its higher Si and Na contents. The observed diffraction intensities of the zagamiite deviate noticeably from the calculated pattern based on the structure reported in [10]. In particular, reflection 002 is markedly more intense than the reflection that was predicted by the synthetic model structure (even with the partial replacement of Ca by Na), whereas reflection 101 is much less intense in the observed pattern than predicted. Similarly, 104, 112, 201, 105, 202, etc., deviate markedly. Therefore, we conducted a LeBail extraction of the apparent $|F(hkl)|$ with an R_p of 5.7% and used reversed Monte Carlo methods [25] for a) global optimization as a check for possible competitive alternative structures, and b) obtaining site distributions within the zagamiite structure (based on the effective electron densities at given sites) through local optimization. The local optimization converged to an R_F of 14.3% (whereas the initial structure model based on the synthetic CAS phase converges to not better than 17%). The final converged structure model was used for a Rietveld refinement of the fractional atomic coordinates and site occupancies of zagamiite. The Rietveld refinement was conducted with Powdercell [26] and GSAS [27] and converged to a wRp of 9.2% (GSAS) and 6.4% (Powdercell) with a reduced χ^2 of 1.4 for 2956 observations. The Pseudovoigt profiles with fixed mixing parameters of $n_a = 0.38$ and $n_b = 0.0$ (fixed) were used, and the profile parameters U , V , and W were refined with Powdercell to 1.220, 0.017, and 0.012, respectively. The frame shown in Figure 3a was used for the Rietveld refinement. After integration with Dioptas [24], the remaining background was fitted with a 5th degree Chebychev polynomial. Stishovite (which is not visible at the surface of the section at that location, but which is present underneath the zagamiite) exhibits the superposition of the coarser crystallites on its Debye rings (Figure 3a). Therefore, for the structural analysis and refinement of the zagamiite, the stishovite was first refined with the Rietveld approach, then with the Pawley approach, and finally the zagamiite was refined with the Rietveld approach, while keeping the model pattern of the stishovite fixed. Thereby, an upper limit of any potential non-powder statistical contribution from the stishovite was fitted before the structure of the zagamiite was analyzed. The Rietveld refinement of the zagamiite converged to a wRp of 6.4% (including background) and is shown in Figure 3b.

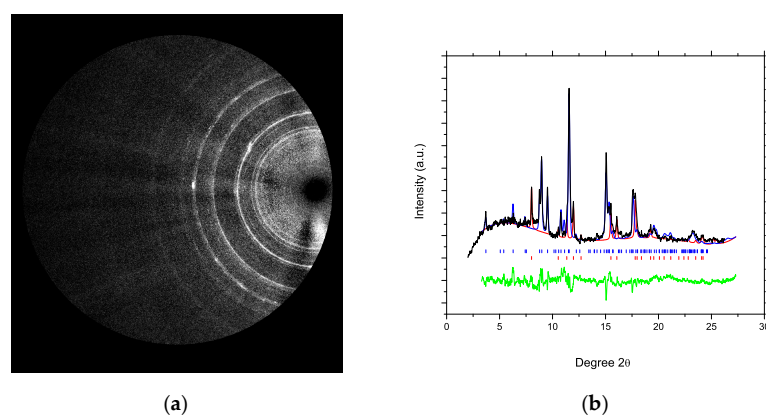


Figure 3. Representative X-ray diffraction pattern from NWA 856. (a) Diffraction image (after subtracting frame collected on maskelynite). The Debye rings of zagamiite are smooth, while the rings of the stishovite are spotty as a result of diffraction from larger crystallites. (b) Integrated pattern. Observed pattern (black), modeled pattern of zagamiite (blue), plus stishovite (red), and residual of fit (green). Because of its coarse, grained fraction, the stishovite was fitted with the Pawley method, then a Rietveld refinement of the zagamiite was conducted. The primary beam wavelength was 0.4133 Å. Blue tick marks indicate reflections of zagamiite; red tick marks indicate reflections of stishovite.

The synchrotron diffraction data confirm that the zagamiite in the NWA 856 assumes hexagonal space group $P6_3/mmc$ with a unit cell of $a = 5.399$ (2) Å, $c = 12.81$ (4) Å, $V = 323.3$ (11) Å³, and $Z = 2$. The fractional atomic coordinates are given in Table 2 and in the supplementary file (crystallographic information file zagamiite.cif). The observed and calculated normalized structure factor moduli of the extracted reflections are given in the supplementary file (crystallographic information file zagamiite.cif). The structures and cell parameters of zagamiite in the NWA856 and in the Zagami are equal within uncertainties.

Table 2. Fractional atomic coordinates, site fractional occupancies, and isotropic thermal displacement factors of type zagamiite in NWA 856. Isotropic displacement parameters are in Å².

Atom	Wyck.	Occ.	x	Y	z	U _{iso}
Ca1	2c	0.80 (7)	1/3	2/3	1/4	0.075 (7)
Na1	2c	0.2 (1)	1/3	2/3	1/4	0.075 (7)
Si1	6g	0.78 (6)	1/2	0	0	0.017 (6)
Al1	4e	0.97 (1)	0	0	0.143 (2)	0.014 (8)
Fe	4e	0.03 (1)	0	0	0.143 (2)	0.014 (8)
Si2	4f	0.3 (2)	2/3	1/3	0.22 (2)	0.011 (5)
Na2	2d	0.1 (1)	1/3	2/3	3/4	0.011 (5)
O1	4f		2/3	1/3	0.078 (1)	0.009 (1)
O2	6h		0.323 (2)	0.1617 (3)	1/4	0.019 (2)
O3	12k		0.183 (2)	0.366 (3)	0.0814 (4)	0.020 (2)

Zagamiite $\text{CaAl}_2\text{Si}_{3.5}\text{O}_{11}$ has a structure very similar to the synthetic hexagonal CAS phase $\text{CaAl}_4\text{Si}_2\text{O}_{11}$. However, it deviates in a few aspects: (1) Site 4f is dominated by Si rather than Al. In the synthetic CAS phase [10], site 4f involves a seemingly unphysical short cation–cation distance. Gautron et al. [10] interpreted site 4f as the average position of a cation (Al or Si) coordinated tetrahedrally by oxygen. In zagamiite, site 4f is occupied by less than 0.5 cations. Thus, there is statistically no competition between cations on this site, and the site is not representing an average of an unresolved disorder (such as in the synthetic CAS phase) but partial occupancy of a well-defined site. (2) In zagamiite, a minor amount of Na may reside on a partially occupied site 2d, which is at half the distance between the partially occupied Si sites 4f. Just as with site 4f itself, the partial occupancies are consistent with the competition between these sites, and no unphysical short distances occur. The higher Si content shortens the T–O distances to 3×1.655 Å + 1×1.844 Å relative to those in the synthetic CAS [10] of 1.699 and 1.877 Å, respectively. Thus, we propose that in zagamiite site T is dominated by Si (not excluding minor Al, but this cannot be assessed from the structure). The Si–O distances for site 6g (M1 in [10]) are equal to those found by Gautron et al. [10] and are unusually long. We propose the same reason as Gautron et al. [10]: bond distances appear extended on average because of the high amount of vacancies on that site. (Al,Fe)–O distances for site 4e (M2 in [10]) are larger in zagamiite than in the synthetic CAS phase by 17% and 30%, probably because of the presence of Fe^{2+} in the zagamiite type material. In zagamiite the (Ca,Na)–O distances are shorter by 5% and 19% than in the CAS phase. With ~10% Na on that site, an expansion of the average bond distance is expected for zagamiite. However, this site is quite anisotropic, and it is proposed that the actual bond coordination of Na is lower than that of Ca for this site.

4. Discussion

4.1. Crystal Chemistry

The structure of zagamiite is built from dioctahedral (Si,Al)O₃ layers with intermittent layers of face-sharing octahedra and tetradecahedral polyhedra that are combinations of trigonal bases with pyramids (Figure 4, [10,16]). The latter are occupied by Ca and alkalis, and the former, face-sharing, inter-layer octahedra are only partially occupied by Al, which is partially replaced by Si and the minor ferric Fe. The structure represents a potentially close packing of Ca–O layers. However, the full occupancy of all sites invokes

unphysically close intercationic distances in the adjacent interlayer polyhedra [10]. Thus, the actual structure is less dense, and the partial filling of sites is the consequence of the mutual exclusion of the occupying adjacent sites, in particular the face-sharing, inter-layer octahedra (indicated by a yellow color in Figure 4). The compositional variation along the zagamiite–donwilhelmsite series and the substitution of the Na are both governed by these steric constraints on site occupancy and the charge balance. The zagamiite type is Na-deficient and slightly Ca-enriched relative to plagioclase, which has the same Al–Si ratio, and is Al-poor but Si-rich relative to donwilhelmsite, $\text{CaAl}_4\text{Si}_2\text{O}_{11}$ [10,20]. Figure 5 shows that the composition of the zagamiite type lies close to the An–Ab join when projected from the Na (~An45), but the Na–Ca ratio (~0.4) is much lower than that of plagioclase (~1.2) with the same Al–Si ratio. This contrasts with tissintite [28] and albitic jadeite [29], which are highly defective clinopyroxenes where the Na–Ca ratios of host maskelynite and pyroxene are nearly equal. Conserving Al and Si between a putative plagioclase (plg) and zagamiite (zag) yields:

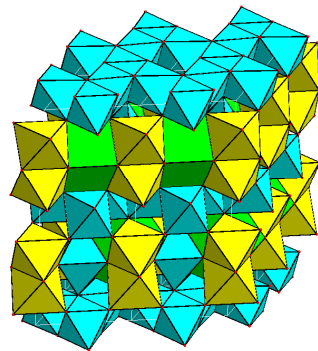
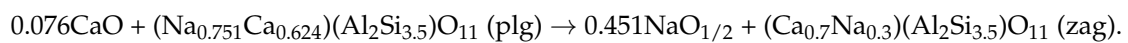


Figure 4. Representation of the structure of zagamiite: Blue: $(\text{Si,Al})\text{O}_3$ -dioctahedral layers. Yellow: Al + Fe face-sharing, inter-layer octahedra. Green: Ca + Na dodecahedral sites. The polyhedra that are represented by yellow and green colors are partially occupied (Table 2).

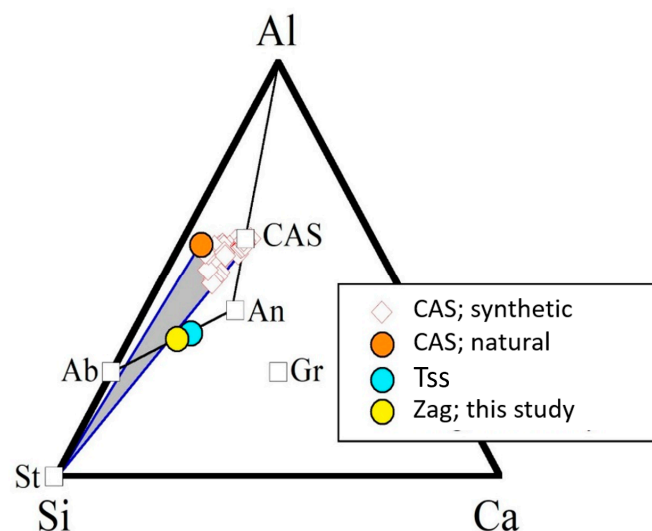


Figure 5. Compositions of meteoritic tissintite (Tss), zagamiite (Zag), and donwilhelmsite ('CAS; natural') [11,28]; this study, and the synthetic CAS phase [9,10] in terms of molar Ca–Al–Si. Endmember compositions of albite (Ab), anorthite (An), CAS (CAS phase), grossular (Gr), and stishovite (St) are also shown. The gray area encloses the region consistent with St + CAS tie lines for plagioclase and plagioclase-like bulk compositions. Zagamiite and tissintite plot on the Ab–An binary when projected from Na, and the CAS phase is significantly away from this joint.

The differences in the chemistry between the zagamiite and donwilhelmsite are accommodated mostly through differing site occupancies of the 12-coordinated 2c ($\text{Ca}_{4/5}\text{Na}_{1/5}$ in zagamiite vs. Ca_1 in donwilhelmsite), octahedral 6g ($\sim\text{Si}_{3/4}\square_{1/4}$ vs. $\text{Si}_{2/3}\text{Al}_{1/3}$), and tetrahedral 4f ($\sim\text{Si}_{1/3}\square_{2/3}$ vs. $\text{Al}_{1/2}\square_{1/2}$) sites with the endmember formula $\text{CaAl}_2\text{Si}_{3.5}\text{O}_{11}$ for zagamiite versus $\text{CaAl}_4\text{Si}_2\text{O}_{11}$ for donwilhelmsite.

Most synthetic CAS phases are solid solutions between donwilhelmsite and zagamiite [7,30–32], with a sodic component that shall be characterized here in more detail. The components are correlated through the coupled substitution of $\text{Ca} + \text{Al} \leftrightarrow \text{Na} + \text{Si}$ [32]. This is shown in Figure 6:

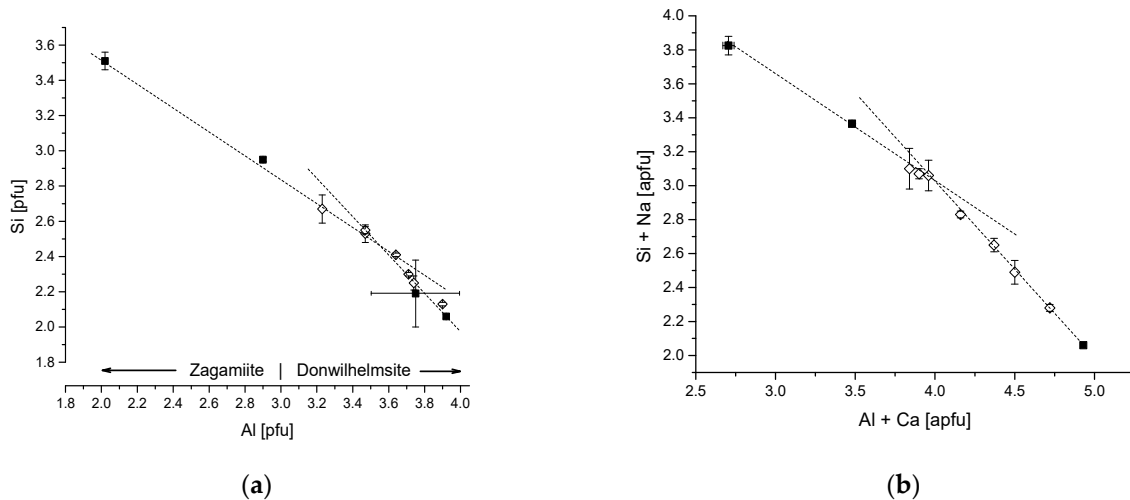


Figure 6. (a) Correlation between Al and Si (atoms per formula unit (apfu)) in the zagamiite–donwilhelmsite pseudobinary system. The boundary between the two minerals is indicated by a bar. Black squares: natural zagamiite (this study and [11]) and donwilhelmsite [20]; the square with the largest uncertainty indicates the variance of both natural and synthetic donwilhelmsite, based on [7]. Hollow diamonds: synthetic CAS phase [32]. The synthetic samples include between 0 and 0.54 apfu Na. (b) The correlation between the sums of atoms per formula unit Al + Ca versus Si + Na. As observed by Akaogi et al. [32], the correlation is strong, but the present extended data set indicates that the slope changes around $\text{Al} + \text{Ca} \sim 4.0$. Dashed lines represent linear fits (see text).

Figure 6 shows that the solid solution mechanism changes above $\text{Si} + \text{Na} \sim 3$ apfu and $\text{Al} + \text{Ca} \sim 4.0$, respectively. The correlations are $[\text{Na} + \text{Si}] = 5.55(7) - 0.63(2)[\text{Ca} + \text{Al}]$ and $7.10(8) - 1.02(2)[\text{Ca} + \text{Al}]$ above and below those values with $R^2 = 0.997$ and 0.998 , respectively. The latter correlation avails for sodic donwilhelmsite and gives an endmember of $\text{NaAl}_3\text{Si}_3\text{O}_{11}$, as specified by Akaogi et al. [32]. The former correlation represents Na substitution in zagamiite and gives an endmember of $\text{Na}_2\text{Al}_2\text{Si}_{3.5}\text{O}_{11}$. The transition between both mechanisms is also apparent in the molar volumes but lacks statistics for assessing the two sodic endmember volumes independently. The solid melt partitioning experiments are consistent with our observation that the zagamiite–donwilhelmsite solid solution is comparatively less compatible for Na than for K and moderately compatible for Mg and Fe (in a MORB bulk composition). The experiments also indicate that zagamiite enriches Sr over Ca and Ba [30].

4.2. Mechanism of Formation

Zagamiite has significant Fe and Mg and a substantial deficit of Na relative to plagioclase of an equivalent Al/Si, suggesting that it formed by crystallization from a melt derived from a plagioclase-rich mixture of plagioclase and clinopyroxene, rather than through the solid-state transformation of a feldspar precursor. Shock peak temperatures during the impact that generated the Zagami shergottite did not exceed 400 K [33]. Shock-induced melting occurred only in so called ‘hot spots’, that is, locations where the shock-induced

temperatures were far beyond those of the Hugoniot of the bulk material. ‘Hot spots’ occur in shocked solid materials through a void collapse or chemical reactions such as the dehydration of low-density minerals [18,34]. The phase diagram of the dry MORB (Figure 7) indicates that the zagamiite formed at or close to the solidus, because this mineral occurs along with stishovite at the rim of quenched melts (Figure 1), and as a single phase within the core of former melt pockets (Figure 2). By contrast, metastable stöfflerite or tissintite occurs further away from the hot spot, and maskelynite is found in the bulk rock whose maximal temperature and pressure are determined by the principal Hugoniot line [2,28]. With zagamiite as a solidus phase, the static phase diagram of the CAS system and the MORB [6,7] places the temperatures and pressures for the formation of this mineral in the Zagami and NWA 856 to 20–23 GPa, 2300–2600 K (Figure 7). These conditions either mark peak pressures for the Zagami and NWA 856 or represent conditions upon release from the peak shock state. An absence of davemaite is either the result of the vitrification of this mineral upon release, a process that has a low kinetic barrier [4], or it marks an upper bound for the peak pressures. However, temperature reduction in local hot spots upon rarefaction (shock release) changes from adiabatic to a rapid quench regime at modest pressures, which allows for the conservation of high-pressure minerals [18,35]. Hence, the formation of zagamiite upon release had to have occurred not far below peak shock pressures and maximal hot spot temperatures. Otherwise, retrograde transformations would have destroyed this mineral.

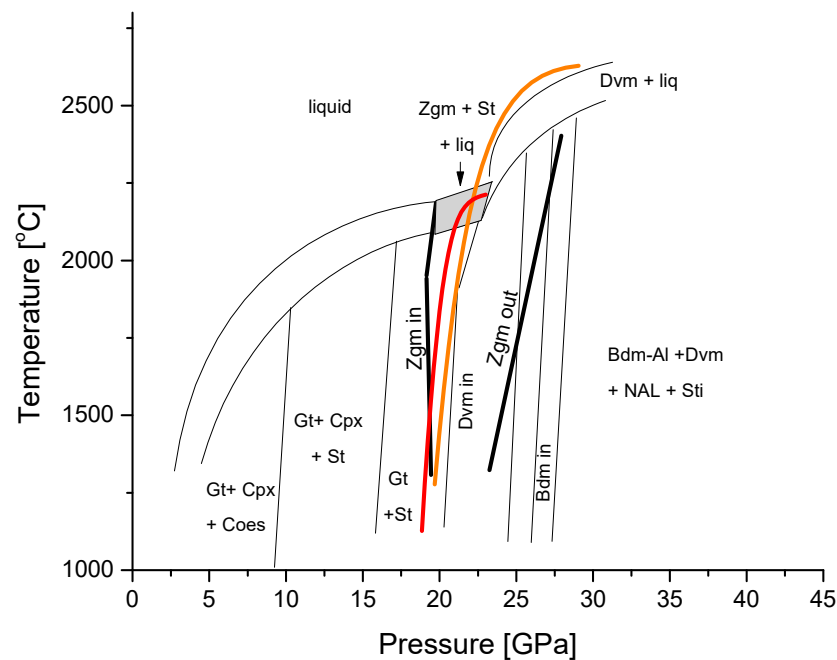


Figure 7. Simplified representation of the phase diagram of the dry MORB [7] as an approximation of the bulk melt pocket composition. Lower and upper bounds of the occurrence of zagamiite and donwilhelmsite are indicated through thick black lines. The coexistence field melt + zagamiite + stishovite is shown as the gray area. Orange curve: approximate release path based on a 29 ± 0.5 GPa peak pressure [33] of the bulk rock of Zagami. Red curve: release path of the hot spot where the zagamiite formed.

The formation of minerals in shock-metamorphic environments can markedly deviate from the static phase boundaries [16,18,34,35]. However, crystallization from the shock-generated melt or at immediate contact with the melt have been found to yield the same phase assemblages as static experiments without much potential for extensive excursion toward higher pressures [33,34]. Peak pressures much beyond the pressures of the thermodynamic phase stability fields are excluded by the accordingly much higher liq-

uidus temperatures, which imply that the pressure–temperature release paths that cross the liquid field prevent the conservation of high-pressure phases like bridgmanite, which has, nevertheless, been observed in these parageneses [35,36]. Thus, minerals like bridgmanite and akimotoite are conserved in shocked meteorites only if the bulk rock has received considerably less heat than the locations where the bridgmanite formed and where the high local temperature decayed rapidly towards the bulk rock release temperature, while the dynamic pressure was still within or not far below the stability field of these high-pressure phases [36]. This point also holds for zagamiite (Figure 7). Thus, zagamiite is defined by its rather narrow stability field within the CAS system and the strong increase in the liquidus above its stability field within an accordingly narrow range of pressure–temperature conditions for the shock melt pockets in which it is observed (Figure 7). The estimate of the Hugoniot peak pressure of the Zagami meteorite material from its shock deformation features is 29 ± 0.5 GPa [33]. This is a few GPa above the pressure obtained from the melt pocket paragenesis in this paper. The observed paragenesis places two constraints on the release path: a peak pressure at temperatures where the interior of the hot spot was fully molten and an absence of garnet in the interior of the melt pockets (the red curve in Figure 7). This implies that the major cooling occurred within or not much below the stability field of the zagamiite and that, afterwards, the temperature was too low to permit back-transformation of this mineral. A peak pressure of 29 GPa cannot be excluded for the melt pocket but implies that the zagamiite had formed within a ns time scale during release (the orange curve in Figure 7).

An offset between the bulk shock and the hot spot peak pressure does not necessarily imply a systematic error in the pressure assessments but indicates that part of the shock energy in the melt was consumed by turbulent mixing and the chemical reaction rather than through dynamic compression. The total energy conservation requires the dynamic pressure of the molten hot spot to be initially lower than that of the surrounding solid material that experiences a ~ 2000 K lower temperature than the hot spot. Within the dynamic compression regime, the phases with a different shock impedance, such as the various bed rock minerals and the shock-generated melt, seek stress homogenization through reverberation, but for the melt phase this process has to involve dissipative motion (a numerical modeling of this process is given in the supplement to [37]). This evolution has remained here far from completion (Figures 1 and 2), in agreement with the rather short shock duration of most shergottites [26,33,35,38]. Thus, the offset of 6–9 GPa between the bulk rock and the melt pocket is conceivably real.

5. Conclusions

Zagamiite is not a rare occurrence in shock melt pockets in the Martian meteorite class of shergottites (see References [2,3,11,14–20]). Constraints on the conditions of its formation are found through the narrow pressure–temperature regime of its formation that is bracketed by total melting at a high temperature, the occurrence of davemaoite at a higher temperature, and that of garnet at a lower pressure. The synthetic and natural CAS phase is actually a solid solution between zagamiite, $\text{CaAl}_2\text{Si}_{3.5}\text{O}_{11}$, and donwillhelmite, $\text{CaAl}_4\text{Si}_2\text{O}_{11}$, and occurs in the liquid–solid coexistence field in MORB-like and in more calcic–alkaline bulk compositions above 20 GPa. These two endmembers involve two different substitutions of the sodic component with endmembers $\text{Na}_2\text{Al}_2\text{Si}_{3.5}\text{O}_{11}$ and $\text{NaAl}_3\text{Si}_3\text{O}_{11}$, respectively. In the Zagami and NWA856, we observed sequences of transformations from the bulk rock maskelynite to zagamiite in the centers of former shock melt pockets via stöfflerite or tissintite at the less strongly heated rims and a zagamiite–stishovite-quenched melt assembly that surrounds the zagamiite. Zagamiite and davemaoite are likewise solidus phases at 20–23 and above 23 GPa, respectively. Therefore, they are expected to have influenced the distribution of elements in a potential deep magma ocean in the early stages of the Earth if this ocean extended to ~ 600 km depth or beyond. For instance, zagamiite enriches K over Na and Sr over Ba. As a result, both minerals operate

as retainers of minor and trace elements that are incompatible in the upper mantle but are trapped by zagamiite or davemaoite as host phases.

Supplementary Materials: The following supporting information can be downloaded at: <https://www.mdpi.com/article/10.3390/min14010018/s1>, crystallographic information file zagamiite.cif.

Author Contributions: Conceptualization, C.M. and O.T.; methodology, C.M., O.T., J.R.B., E.G. and V.B.P.; software, E.G.; validation, C.M. and O.T.; data curation, C.M., O.T. and V.B.P.; writing—original draft preparation, C.M. and O.T.; writing—review and editing: all authors. All authors have read and agreed to the published version of this manuscript.

Funding: SEM, EBSD, and EPMA analyses were carried out at the Caltech GPS Division Analytical Facility, which is supported, in part, by NSF Grants EAR-0318518 and DMR-0080065. O.T. acknowledges support by NSF EAR-1838330. The publication fees for this article were supported by the UNLV University Libraries Open Article Fund. GSECARS is supported through DOE Award DESC0005278 and NSF awards EAR-1128799,-0318518, DE-FG02-94ER14466, and DMR-0080065. The Advanced Photon Source, a DOE Office of Science User Facility, is operated by Argonne National Laboratory under Contract No. DE-AC02-06CH11357.

Data Availability Statement: All relevant data are provided in the paper. In addition, a crystallographic information file of zagamiite is provided as a supplement. This file includes a table of the $|F(hkl)|$ of type zagamiite. Diffraction frames are stored at the APS-ANL and are made available upon request.

Acknowledgments: We would like to thank the three reviewers and the academic editor for their very helpful comments.

Conflicts of Interest: The authors declare no conflict of interest. The funders had no role in the design of the study; in the collection, analyses, or interpretation of the data; in the writing of the manuscript; or in the decision to publish these results.

References

- Gillet, P.; Chen, M.; Dubrovinsky, L.; El Goresy, A. Natural NaAlSi₃O₈-hollandite in the shocked Sixiangkou meteorite. *Science* **2000**, *287*, 1633–1636. [[CrossRef](#)] [[PubMed](#)]
- Tschauner, O.; Ma, C.; Spray, J.G.; Greenberg, E.; Prakapenka, V.B. Stöfflerite, (Ca,Na)(Si,Al)₄O₈ in the hollandite structure: A new high-pressure polymorph of anorthite from martian meteorite NWA 856. *Am. Min.* **2021**, *106*, 650–655. [[CrossRef](#)]
- Ma, C.; Tschauner, O.; Beckett, J.R.; Rossman, G.R.; Prescher, C.; Prakapenka, V.B. Liebermannite, KAlSi₃O₈, a new shock-metamorphic, high-pressure mineral from the Zagami Martian meteorite. *Met. Planet. Sci.* **2018**, *53*, 50–61. [[CrossRef](#)]
- Tschauner, O.; Huang, S.; Yang, S.C.; Humayun, M.; Liu, W.J.; Corder, S.N.G.; Bechtel, H.A.; Tischler, J.; Rossman, G.R. Discovery of davemaoite, CaSiO₃-perovskite, as a mineral from the lower mantle. *Science* **2021**, *374*, 891–894. [[CrossRef](#)] [[PubMed](#)]
- Liu, L.G. High-pressure phase-transformations of albite, jadeite and nepheline. *Earth Planet. Sci. Lett.* **1978**, *37*, 438–444. [[CrossRef](#)]
- Irifune, T.; Ringwood, A.E.; Hibberson, W.O. Subduction of continental crust and terrigenous and pelagic sediments: An experimental study. *Earth Planet. Sci. Lett.* **1994**, *126*, 351–368. [[CrossRef](#)]
- Liu, X.; Ohfuji, H.; Nishiyama, N.; He, Q.; Sanehira, T.; Irifune, T. High-P behavior of anorthite composition and some phase relations of the CaO-Al₂O₃-SiO₂ system to the lower mantle of the Earth, and their geophysical implications. *J. Geophys. Res. Sol. Earth* **2021**, *117*, B9.
- Gautron, L.; Kesson, S.E.; Hibberson, W.O. Phase relations for CaAl₂Si₂O₈ (anorthite composition) in the system CaO-Al₂O₃-SiO₂ at 14 GPa. *Phys. Earth Planet. Int.* **1996**, *97*, 71–81. [[CrossRef](#)]
- Gautron, L.; Fitz Gerald, J.D.; Kesson, S.E.; Eggleton, R.A.; Irifune, T. Hexagonal Ba-ferrite: A good model for the crystal structure of a new high-pressure phase CaAl₄Si₂O₁₁. *Phys. Earth Planet. Int.* **1997**, *102*, 223–229. [[CrossRef](#)]
- Gautron, L.; Angel, R.J.; Miletich, R. Structural characterization of the high-pressure phase CaAl₄Si₂O₁₁. *Phys. Chem Min.* **1999**, *27*, 47–51. [[CrossRef](#)]
- Beck, P.; Gillet, P.; Gautron, L.; Daniel, I.; El Goresy, A. A new natural high-pressure (Na,Ca)-hexaluminosilicate [(Ca_xNa_{1-x})Al_{3+x}Si_{3-x}O₁₁] in shocked Martian meteorites. *Earth Planet. Sci. Lett.* **2004**, *219*, 1–12. [[CrossRef](#)]
- Ma, C.; Tschauner, O.; Beckett, J.R. A new high-pressure calcium aluminosilicate (CaAl₂Si_{3.5}O₁₁) in martian meteorites: Another after-life for plagioclase and connections to the CAS phase. In Proceedings of the 48th Lunar and Planetary Science Conference Abstract 1128, Houston, TX, USA, 20–24 March 2017.
- Ma, C.; Tschauner, O. Zagamiite, IMA 2015-022a. CNMNC Newsletter No. 36, April 2017. *Min. Mag.* **2017**, *81*, 403–409.
- Ma, C. A closer look at shocked meteorites: Discovery of new high-pressure minerals. *Am. Min.* **2018**, *103*, 1521–1522. [[CrossRef](#)]
- Chen, D.L.; Zhang, A.C.; Pang, R.-L.; Chen, J.-N.; Li, Y. Shock-induced phase transformation of anorthitic plagioclase in the eucrite meteorite Northwest Africa 2650. *Met. Planet. Sci.* **2019**, *54*, 1548–1562. [[CrossRef](#)]

16. Tschauner, O. High-pressure minerals. *Am. Min.* **2019**, *104*, 1701–1731. [[CrossRef](#)]
17. Yoshida, M.; Miyahara, M.; Suga, H.; Yamaguchi, A.; Tomioka, N.; Sakai, T.; Ohfuji, H.; Maeda, F.; Ohira, I.; Ohtani, E.; et al. Elucidation of impact event recorded in the lherzolitic shergottite NWA 7397. *Met. Planet. Sci.* **2021**, *59*, 1729–1743. [[CrossRef](#)]
18. Tschauner, O.; Ma, C. Discovering High-Pressure and High-Temperature Minerals. In *Celebrating the International Year of Mineralogy*, 3rd ed.; Bind, L., Cruciani, G., Eds.; Springer Mineralogy: New York, NY, USA; Springer: Berlin, Germany, 2023; pp. 154–196.
19. Morrison, S.M.; Prabhu, A.; Hazen, R.M. An evolutionary system of mineralogy, Part VI: Earth's earliest Hadean crust (>4370 Ma). *Am. Min.* **2023**, *108*, 43–58. [[CrossRef](#)]
20. Fritz, J.; Greshake, A.; Klementova, M.; Wirth, R.; Palatinus, L.; Trønnes, R.G.; Fernandes, V.A.; Böttger, U.; Ferrière, L. Donwilhelmsite, $[\text{CaAl}_4\text{Si}_2\text{O}_{11}]$, a new lunar high-pressure Ca-Al-silicate with relevance for subducted terrestrial sediments. *Am. Min.* **2020**, *105*, 1704–1711. [[CrossRef](#)]
21. Armstrong, J.T. CITZAF: A package of correction programs for the quantitative electron microbeam X-ray analysis of thick polished materials, thin films, and particles. *Microbeam Anal.* **1995**, *4*, 177–200.
22. Ma, C.; Beckett, J.R. A new type of tissintite, $(\text{Ca,Mg,Na},\square_{0.14})(\text{Al,Fe,Mg})\text{Si}_2\text{O}_6$, in the Zagami martian meteorite: A high-pressure clinopyroxene formed in shock. In Proceedings of the 48th Lunar and Planetary Science Conference 2017, Abstract 1639, Houston, TX, USA, 20–24 March 2017.
23. Dera, P.; Zhuravlev, K.; Prakapenka, V.B.; Rivers, M.L.; Finkelstein, G.J.; Lavina, B.; Grubor-Urošević, O.; Tschauner, O.; Clark, S.M.; Downs, R.T. High pressure single-crystal micro X-ray diffraction analysis with GSE_ADA/RSV software. *High Press. Res.* **2013**, *34*, 1–19. [[CrossRef](#)]
24. Prescher, C.; Prakapenka, V.B. DIOPTAS: A program for reduction of two-dimensional X-ray diffraction data and data exploration. *High Press. Res.* **2015**, *35*, 223–230. [[CrossRef](#)]
25. Putz, H.; Schön, J.C.; Jansen, M. Combined method for ab initio structure solution from powder diffraction data. *J. Appl. Cryst.* **1999**, *32*, 864–870. [[CrossRef](#)]
26. Kraus, W.; Nolze, G. PowderCell—A program for the representation and manipulation of crystal structures and calculation of the resulting X-ray powder patterns. *J. Appl. Cryst.* **1996**, *29*, 301–303. [[CrossRef](#)]
27. von Dreele, R.B.; Larson, A.C. General Structure Analysis System (GSAS). *Los Alamos Natl. Lab. Rep. LAUR* **2004**, *748*, 86–748.
28. Ma, C.; Tschauner, O.; Beckett, J.R.; Liu, Y.; Rossman, G.R.; Zhuravlev, K.; Prakapenka, V.B.; Dera, P.; Taylor, L.A. Tissintite, $(\text{Ca,Na},\square)\text{AlSi}_2\text{O}_6$, a highly-defective, shock-induced, high-pressure clinopyroxene in the Tissint martian meteorite. *Earth Planet. Sci. Lett.* **2015**, *422*, 194–205. [[CrossRef](#)]
29. Ma, C.; Tschauner, O.; Kong, M.; Beckett, J.R.; Greenberg, E.; Prakapenka, V.B.; Lee, Y. A high-pressure, clinopyroxene-structured polymorph of albite in highly shocked terrestrial and meteoritic rocks. *Am. Min.* **2022**, *107*, 625–630. [[CrossRef](#)]
30. Hirose, K.; Shimizu, N.; van Westrenen, W.; Fei, Y.W. Trace element partitioning in Earth's lower mantle and implications for geochemical consequences of partial melting at the core-mantle boundary. *Phys. Earth Planet. Int.* **2004**, *146*, 249–261. [[CrossRef](#)]
31. Nishi, M.; Gréaux, S.; Tateno, S.; Kuwayama, Y.; Kawai, K.; Irifune, T.; Maruyama, S. High-pressure phase transitions of anorthosite crust in the Earth's deep mantle. *Geosci. Front.* **2018**, *9*, 1859–1870. [[CrossRef](#)]
32. Akaogi, M.; Haraguchi, M.; Nakanishi, K.; Ajiro, H.; Kojitani, H. High-pressure phase relations in the system $\text{Ca Al}_4\text{Si}_2\text{O}_{11}$ – $\text{Na Al}_3\text{Si}_3\text{O}_{11}$ with implications for Na-rich CAS phase in shocked Martian meteorites. *Earth Planet. Sci. Lett.* **2010**, *289*, 503–508. [[CrossRef](#)]
33. Fritz, J.; Artemieva, N.; Greshake, A. Ejection of Martian meteorites. *Met. Planet. Sci.* **2005**, *40*, 1393–1411. [[CrossRef](#)]
34. Hu, J.P.; Sharp, T.G. Back-transformation of high-pressure minerals in shocked chondrites: Low-pressure mineral evidence for strong shock. *Geochim. Cosmochim. Acta* **2017**, *215*, 277–294. [[CrossRef](#)]
35. Ma, C.; Tschauner, O.; Beckett, J.R.; Liu, Y.; Rossman, G.R.; Sinogeikin, S.V.; Smith, J.S.; Taylor, L.A. Ahrensite, $\gamma\text{-Fe}_2\text{SiO}_4$, a new shock-metamorphic mineral from the Tissint meteorite: Implications for the Tissint shock event on Mars. *Geochim. Cosmochim. Acta* **2016**, *184*, 240–256. [[CrossRef](#)]
36. Tschauner, O.; Ma, C.; Beckett, J.R.; Prescher, C.; Prakapenka, V.B.; Rossman, G.R. Discovery of bridgmanite, the most abundant mineral in earth, in a shocked meteorite. *Science* **2014**, *6213*, 1100–1102. [[CrossRef](#)] [[PubMed](#)]
37. Adcock, C.; Tschauner, O.; Hausrath, E.; Hausrath, E.M.; Udry, A.; Luo, S.N.; Cai, Y.; Ren, M.; Ianzirrotti, A.; Newville, M. Shock-transformation of whitlockite to merrillite and the implications for meteoritic phosphate. *Nat. Commun.* **2017**, *8*, 14667. [[CrossRef](#)]
38. Beck, P.; Gillet, P.; El Goresy, A.; Mostefaoui, S. Timescales of shock processes in the solar system from mineralogical transformations in Chondrites and Martian meteorites. *Nature* **2005**, *435*, 1071–1107. [[CrossRef](#)]

Disclaimer/Publisher's Note: The statements, opinions and data contained in all publications are solely those of the individual author(s) and contributor(s) and not of MDPI and/or the editor(s). MDPI and/or the editor(s) disclaim responsibility for any injury to people or property resulting from any ideas, methods, instructions or products referred to in the content.